

Showcasing research from Professor Binghui Xu's laboratory, Institute of Materials for Energy and Environment, College of Materials Science and Engineering, Qingdao University, Qingdao 266071, China.

Synthesis of a MOF-derived magnetite quantum dots on surface modulated reduced graphene oxide composite for high-rate lithium-ion storage

Reactions between 1,3,5-benzenetricarboxylic acid (H<sub>3</sub>BTC), tea polyphenol (TP), graphene oxide (GO) and iron foils are triggered under mild aqueous conditions. Both H<sub>3</sub>BTC and TP are decorated on the surface of GO sheets by  $\pi$ - $\pi$  conjugation while the redox reaction between Fe and GO takes place. The coordination between Fe<sup>3+</sup> and BTC<sup>3-</sup> leads to *in situ* crystallization of Fe-BTC metal-organic framework (MOF) on the surface of the TP-decorated reduced graphene oxide (TP-RGO), both the size of Fe-BTC MOF domains and the restacking of TP-RGO sheets are significantly controlled.

### As featured in:



See Binghui Xu *et al.*,  
*RSC Appl. Interfaces*, 2024, 1, 233.







(4 0 0), (4 2 2), (5 1 1), and (4 4 0), respectively. The characterization peak of RGO can also be seen without any diffraction peaks of other possible impurities.

The FTIR analysis result of the Fe-BTC/TP-RGO sample is shown in Fig. 2a. The sharp peak at about  $3388\text{ cm}^{-1}$  is attributed to free O–H bonds in the structure. The bands at  $2852\text{ cm}^{-1}$ ,  $1097\text{ cm}^{-1}$  and  $1636\text{ cm}^{-1}$  are attributed to the stretching vibrational peaks of C–H, C–O–C and C=C, while the peaks at  $1636$  and  $1386\text{ cm}^{-1}$  belong to aromatic C=C bonds and C–OH bonds, respectively.<sup>35,36</sup> Moreover, the characteristic peak at  $532\text{ cm}^{-1}$  is related to Fe–O stretching vibrations.

In Fig. 2b, two main Raman peaks of the D-band ( $1325\text{ cm}^{-1}$ ) and G-band ( $1590\text{ cm}^{-1}$ ) can be seen for the Fe-BTC/TP-RGO and  $\text{Fe}_3\text{O}_4$  QDs@C/RGO samples. The D-band corresponds to the defective and disordered part of the  $\text{sp}^3$  carbon, while the G-band is associated with the ordered  $\text{sp}^2$  carbon.<sup>37,38</sup> The integral intensity ratio of the D-band and G-band is another feature of the Raman spectrum, which provides useful information about the degree of carbon

disorder. The intensity ratios  $I_D$  and  $I_G$  are measured to be 0.94 and 0.64 for the two samples, indicating fewer defects and a high degree of carbon order after thermal treatment. It can be revealed that with the presence of the surface-decorated TP, the conjugated electronic structure of the RGO sheets is repaired during the thermal treatment. Moreover, the large amount of ligand BTC pyrolyzed carbon also accounts for the high graphitization degree of the  $\text{Fe}_3\text{O}_4$  QDs@C/RGO sample.

Fig. 2c exhibits the TGA and DTG curves of the  $\text{Fe}_3\text{O}_4$  QDs@C/RGO sample. From the TGA curve, the initial weight loss that occurred from  $30^\circ\text{C}$  to  $100^\circ\text{C}$  is ascribed to the evaporation of water. The subsequent weight loss mainly occurs between  $300^\circ\text{C}$  and  $600^\circ\text{C}$ , which can be attributed to the oxidation of  $\text{Fe}_3\text{O}_4$  to  $\text{Fe}_2\text{O}_3$  and the decomposition of pyrolytic carbon. The mass loss of the  $\text{Fe}_3\text{O}_4$  QDs@C/RGO sample can be divided into two stages, probably originating from the decomposition of the organic pyrolyzed carbon and RGO sheets. From the corresponding DTG curve, the inflection points of the two stages are measured to be  $369.2$

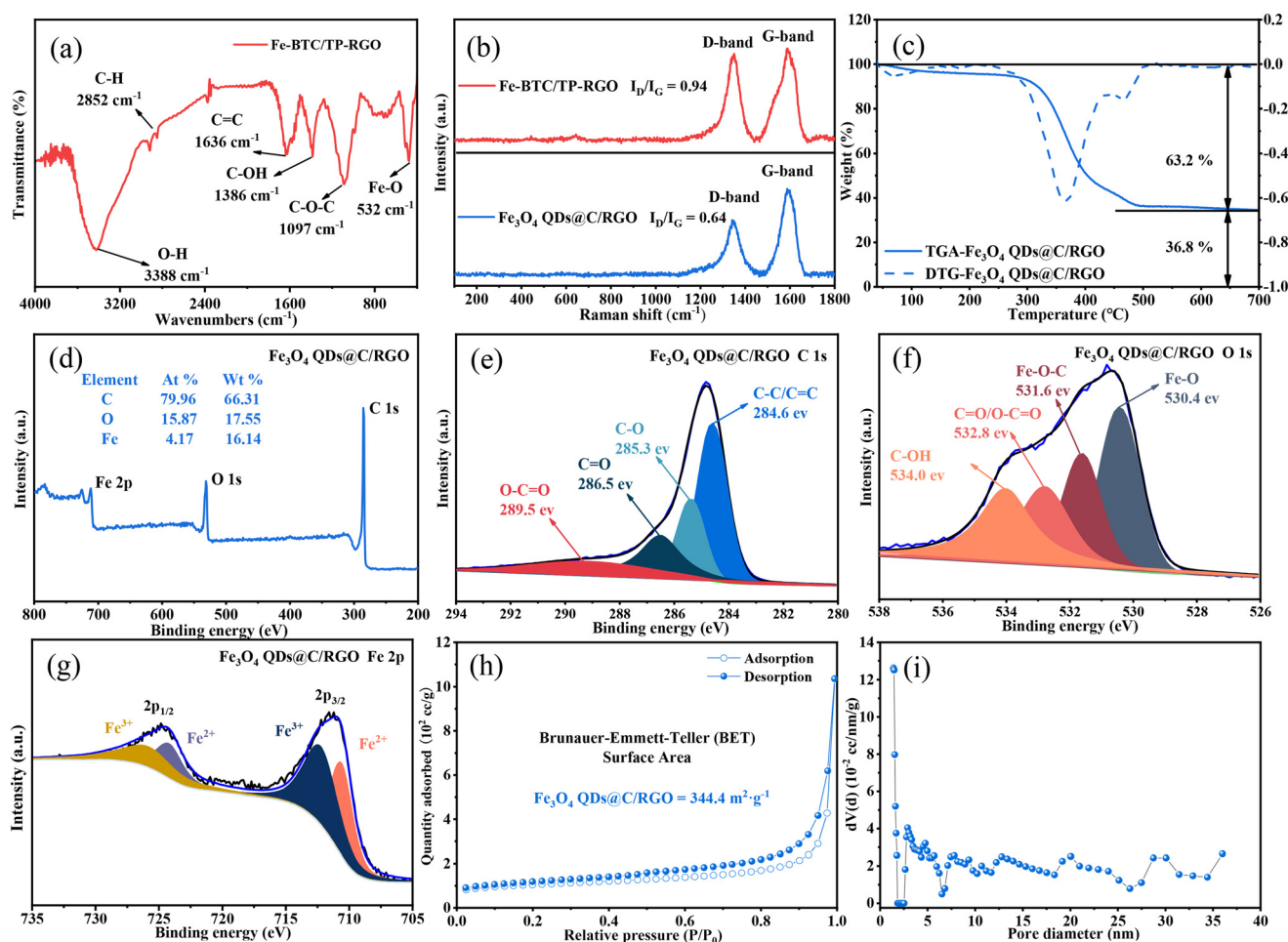


Fig. 2 FTIR pattern (a) of the Fe-BTC/TP-RGO sample. Raman spectra (b) of the Fe-BTC/TP-RGO and  $\text{Fe}_3\text{O}_4$  QDs@C/RGO samples. TGA and DTG curves (c) of the  $\text{Fe}_3\text{O}_4$  QDs@C/RGO sample. Survey XPS spectrum with atomic percentage summary (d). High-resolution C 1s (e), O 1s (f), Fe 2p (g) XPS spectra for the  $\text{Fe}_3\text{O}_4$  QDs@C/RGO sample.  $\text{N}_2$  adsorption and desorption isotherms (h) and pore size distribution (i) of the  $\text{Fe}_3\text{O}_4$  QDs@C/RGO sample.









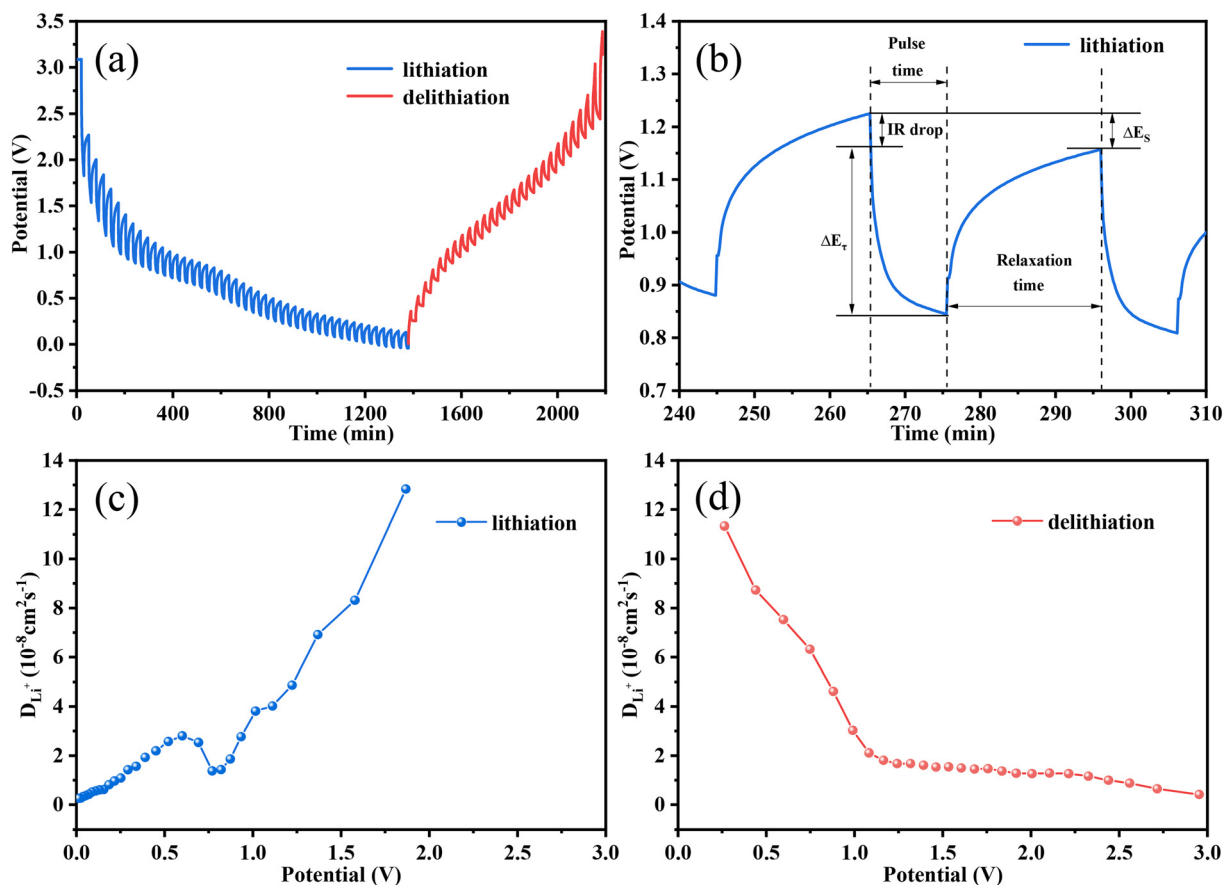


Fig. 6 GITT curves (a) and a profile for a single GITT test (b), and variation of the  $D_{Li^+}$  values during lithiation (c) and delithiation (d) processes of the  $Fe_3O_4$  QDs@C/RGO electrode.

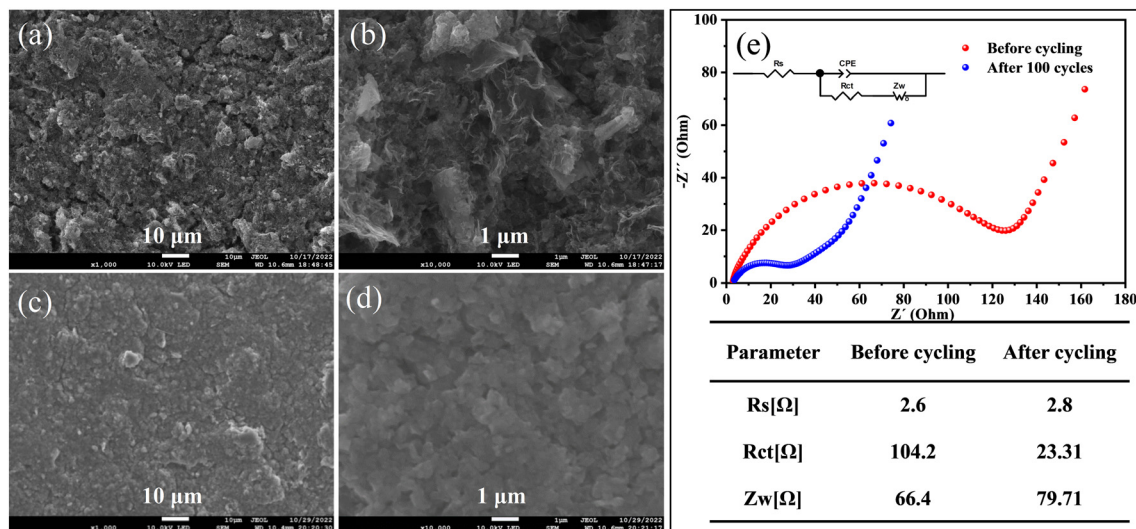


Fig. 7 FESEM images of the  $Fe_3O_4$  QDs@C/RGO electrode before cycling (a and b) and after 100 cycles (c and d) under various magnifications. Nyquist plots of the  $Fe_3O_4$  QDs@C/RGO electrode before cycling and after 100 cycles with inset showing equivalent circuit and the corresponding fitted values of the parameters (e).

excellent structural stability for the composite over long-time cycling. From Fig. 8d, the full cell still exhibits a high reversible capacity of about  $717.29 \text{ mA h g}^{-1}$  after 150 cycles under a current density of  $200 \text{ mA g}^{-1}$ .

## 4. Conclusions

In a mild aqueous reaction system containing  $H_3BTC$ , TP, GO, and iron foils, an Fe-BTC/TP-RGO precursor sample with





- 64 Q. Wei, H. Zhu, S. Yu, G. Xu, J. Yin, J. Tong, T. Chen, X. He, P. Guo, H. Jiang, J. Li and Y. Wang, *Appl. Surf. Sci.*, 2023, **608**, 155093.
- 65 F. Shi, Q. Liu, Z. Jin, G. Huang, B. Xing, J. Jia and C. Zhang, *J. Alloys Compd.*, 2022, **890**, 161911.
- 66 V. Augustyn, J. Come, M. A. Lowe, J. W. Kim, P. L. Taberna, S. H. Tolbert, H. D. Abruna, P. Simon and B. Dunn, *Nat. Mater.*, 2013, **12**, 518–522.
- 67 Q. Chen, W. Zhong, J. Zhang, C. Gao, W. Liu, G. Li and M. Ren, *J. Alloys Compd.*, 2019, **772**, 557–564.
- 68 V. Augustyn, P. Simon and B. Dunn, *Energy Environ. Sci.*, 2014, **7**, 1597.
- 69 Z. Liu, L. Liu, Z. Zhao, J. He, S. Wang and C. Xiong, *Appl. Surf. Sci.*, 2020, **526**, 146639.
- 70 J. Song, Y. Li, X. Lu, W. Zhang, Y. Xiang, J. Chen and Q. Tian, *Appl. Surf. Sci.*, 2022, **604**, 154502.
- 71 B. Yin, X. Cao, A. Pan, Z. Luo, S. Dinesh, J. Lin, Y. Tang, S. Liang and G. Cao, *Adv. Sci.*, 2018, **5**, 1800829.
- 72 C. Lv, C. Lin and X. S. Zhao, *Adv. Energy Mater.*, 2021, **12**, 2102550.
- 73 H. Zhang, P. Zong, M. Chen, H. Jin, Y. Bai, S. Li, F. Ma, H. Xu and K. Lian, *ACS Nano*, 2019, **13**, 3054–3062.
- 74 Y. Cheng, S. Wang, L. Zhou, L. Chang, W. Liu, D. Yin, Z. Yi and L. Wang, *Small*, 2020, **16**, e2000681.
- 75 R. Ding, J. Zhang, J. Qi, Z. Li, C. Wang and M. Chen, *ACS Appl. Mater. Interfaces*, 2018, **10**, 13470–13478.
- 76 Y. Xie, Y. Qiu, L. Tian, T. Liu and X. Su, *J. Alloys Compd.*, 2022, **894**, 162384.
- 77 H. Li, J. Wang, Y. Li, Y. Zhao, Y. Tian, I. Kurmanbayeva and Z. Bakenov, *J. Electroanal. Chem.*, 2019, **847**, 113240.
- 78 Y. Zhao, X. Zhai, D. Yan, C. Ding, N. Wu, D. Su, Y. Zhao, H. Zhou, X. Zhao, J. Li and H. Jin, *Electrochim. Acta*, 2017, **243**, 18–25.

